



# Microstructure and Properties of Electrodeposited nc-TiO<sub>2</sub>/Ni–Fe and Ni–Fe Coatings

P. Ledwig<sup>1</sup> · T. Ratajski<sup>1</sup> · P. Indyka<sup>2</sup> · I. Kalemba-Rec<sup>1</sup> · A. Kopia<sup>1</sup> · M. Kąc<sup>3</sup> · B. Dubiel<sup>1</sup>

Received: 20 June 2019 / Accepted: 5 September 2019 / Published online: 22 September 2019  
© The Author(s) 2019

## Abstract

In this study, nc-TiO<sub>2</sub>/Ni–Fe composite coatings, and Ni–Fe alloys as equivalents to their matrices, were obtained from citrate-sulphate baths in the electrodeposition process using direct current and pulse current conditions. The aim of the study was to examine the effects of TiO<sub>2</sub> nanoparticles and current conditions on the chemical composition, surface morphology, microstructure, microhardness and magnetic properties of the electrodeposited coatings. The results show that the concentration of Fe in Ni–Fe alloys is related to the current conditions and is higher in the case of pulse current electrodeposition, while such a relationship was not observed for composites. The reinforcement of composites with TiO<sub>2</sub> nanoparticles results in a more developed surface topography with many nodule-like structures. Composites and equivalent alloys deposited in pulse current are characterized by a finer grain size than those obtained in direct current. TiO<sub>2</sub> nanoparticles and their agglomerates, several tens of nanometres in size, are distributed randomly in the Ni–Fe matrix of composites deposited in both current conditions used. Incorporation of a high volume fraction of nc-TiO<sub>2</sub>, exceeding over a dozen percent, and decreasing the nanograin size in nc-TiO<sub>2</sub>/Ni–Fe composites electrodeposited under pulse current conditions, allow a higher hardness to be achieved than in their counterparts obtained using direct current. Magnetic measurements showed ferromagnetic ordering of pristine TiO<sub>2</sub> nanoparticles, however, the introduction of TiO<sub>2</sub> nanoparticles into the Ni–Fe matrix resulted in a decrease in coercivity and saturation magnetization.

**Keywords** TiO<sub>2</sub>/Ni–Fe composites · Electrodeposition · Nanostructure · Microhardness · Magnetic properties

## 1 Introduction

Electrodeposition methods are used on a large scale for manufacturing alloy and composite coatings [1]. Additionally, electrodeposition is a suitable method for obtaining nanostructured composites, which are characterized by improved mechanical properties when compared to coarse-grained counterparts [2].

Electrodeposited metal-matrix composites (MMC) strengthened by ceramic particles are of considerable

research interest due to their high hardness, good mechanical, tribological and corrosion resistance properties. Ni–Fe-based composites are also characterized by interesting magnetic and catalytic properties, thus can be used as magnetic sensors in microelectromechanical systems (MEMS), components of magnetic recording devices and magnetic refrigeration systems, as well as hydrogen (HER) and oxygen (OER) generation electrodes [2].

The co-deposition of Fe and Ni is a typical anomalous deposition, where less noble Fe is deposited preferentially before nobler Ni in most electrochemical conditions [3, 4]. Using a single-bath electrochemical process with different deposition parameters, it is possible to obtain materials characterized by various chemical compositions [1, 5].

In addition, the excellent soft ferromagnetic properties of Ni–Fe alloys for recording, storage and memory devices in the computer industry, storage chokes or measurement transducers is crucial. The mechanical properties of such alloys are often insufficient, but can be improved through reinforcement by ceramic particles, such as TiO<sub>2</sub>.

✉ B. Dubiel  
bdubiel@agh.edu.pl

<sup>1</sup> Faculty of Metals Engineering and Industrial Computer Science, AGH University of Science and Technology, al. Adama Mickiewicza 30, 30-059 Kraków, Poland

<sup>2</sup> Faculty of Chemistry, Jagiellonian University, ul. Gronostajowa 2, 30-387 Kraków, Poland

<sup>3</sup> Institute of Nuclear Physics, Polish Academy of Sciences, ul. Radzikowskiego 152, 31-342 Kraków, Poland

Magnetic properties depend on the microstructure and phase composition. The microstructure of electrodeposited Ni–Fe alloys containing below 58 at% of Fe consists of a single phase, being a solid solution with a face-centred cubic structure (fcc). For Fe concentration above 65 at%, the only phase is a solid solution with a body-centred cubic structure (bcc). Between 58 and 65 at% of Fe, both phases are present [6]. Ni–Fe alloys with fcc structure, containing 20–50 at% of Fe are known as permalloys, and are characterized by very high magnetic permeability, low coercivity, high magnetization saturation [7] and high Curie temperature. Their magnetic properties depend on many factors, such as chemical composition, size and orientation of grains, internal stresses or coating thickness [8]. The results obtained by Pavithra et al. revealed a significant impact of the nanocrystalline structure and phase composition on the coercivity and saturation magnetization of electrodeposited Fe–Ni alloys [9]. The addition of nc-TiO<sub>2</sub> particles to the Fe–Ni matrix not only improves the mechanical properties, but also significantly affects the magnetic properties, leading to a decrease in saturation magnetization and increase in coercivity values [10]. Electrodeposition is one of the methods suitable to obtaining MMC composites. It was reported in the literature that electrodeposited composite coatings containing ZrO<sub>2</sub> nanoparticles in the Ni–Fe matrix possessed superior hardness in comparison with parent alloy [11]. Moreover, electrodeposited nickel-based nanocomposites containing various ceramic particles have been extensively investigated. The general aspects related to the mechanisms of their electrodeposition, different parameters affecting the process as well as characterization techniques of nanostructured nickel-ceramic composite coatings were discussed in review paper by Ahmad et al. [12]. However, to our knowledge, studies elaborating the synthesis of TiO<sub>2</sub>/Ni–Fe composites are rare [10, 13].

Bulk TiO<sub>2</sub> is paramagnetic material with a susceptibility of  $\chi = + 5.9 \times 10^{-6} \text{ cm}^3/\text{mol}$ . However, ferromagnetic behaviour is observed in undoped TiO<sub>2</sub> nanostructures, such as thin films [14] and nanoparticles [15, 16]. Although the mechanism for ferromagnetism observed in oxide semiconductors still remains unclear, the origin of this behaviour is usually connected with a high defect concentration. In TiO<sub>2</sub>, defects related to the Ti and O vacancies are considered to be responsible for the room temperature ferromagnetism. Missing oxygen surface atoms in the chemical bonds result in the appearance of unpaired electron spins and superexchange interaction which stabilize ferromagnetic ordering [16, 17]. Because of the short-range interaction between defects, a high concentration of them is needed for realizing room temperature ferromagnetism. On the other hand, a decrease in defect concentration caused, for example, by annealing can reduce ferromagnetic behaviour [16, 18].

Consequently, considering improvements in the hardness while maintaining good ferromagnetic properties, similar to those of Ni–Fe alloys, our research efforts are focused on the synthesis as well as characterization of the microstructure and properties of new nc-TiO<sub>2</sub>/Ni–Fe composites electrodeposited from a single citrate-sulphate bath. The effect of DC and PC current conditions on the chemical composition, surface morphology and microstructure of composites, as well as analogical Ni–Fe alloy coatings, is examined. Moreover, the hardness and magnetic properties are also investigated to evaluate whether the expected combination of properties has been achieved for the fabricated composites.

## 2 Materials and Methods

The chemical composition of the electrolytic bath used in our experiments is given in Table 1. The Ni:Fe ratio in the bath was equal to 14:1. NiSO<sub>4</sub>, NiCl<sub>2</sub> and FeSO<sub>4</sub> were used as the sources of Ni<sup>2+</sup> and Fe<sup>2+</sup> ions. Citric acid was introduced as a buffer and complexing agent. L-Ascorbic acid was used as an anti-oxidative agent to prevent the oxidation of Fe<sup>2+</sup> to Fe<sup>3+</sup>. Sodium lauryl sulphate was added in order to decrease the surface tension of the electrolyte on the phase boundaries. In the electrodeposition of nanocomposites, nc-TiO<sub>2</sub> delivered by Sigma Aldrich (USA) with the concentration in baths of 10 g/L was used. The equivalent diameter of nc-TiO<sub>2</sub> was in the range of 15–40 nm. It was confirmed by electron diffraction that nc-TiO<sub>2</sub> is a mixture of anatase and rutile [19].

For electrodeposition, an Autolab PGSTAT 302N potentiostat/galvanostat (Metrohm, Switzerland) working in three electrode modes was used. Rectangular copper plates with dimensions of 15 mm × 30 mm × 1 mm were applied as a substrate. Before deposition, the plates were ground using water sandpaper up to 4000 grit and subsequently polished with a 1 μm grade Al<sub>2</sub>O<sub>3</sub> suspension. In order to remove solid pollutions, the plates were washed using distilled water, cleaned in ethanol in an ultrasound cleaner and degreased in

**Table 1** Chemical composition of the electrolytic bath

Compound	Concentration (g/L)
NiSO <sub>4</sub> ·7H <sub>2</sub> O	200
NiCl <sub>2</sub> ·6H <sub>2</sub> O	45
FeSO <sub>4</sub> ·7H <sub>2</sub> O	20
Sodium citrate	35
L-Ascorbic acid	1
Sodium lauryl sulphate	0.5
NaOH	To adjust pH to 4
nc-TiO <sub>2</sub>	0; 10

acetone. A platinum plate was used as the counter electrode and saturated Ag/AgCl as the reference electrode. Before the deposition the electrolytic baths with nc-TiO<sub>2</sub> particles were sonicated by 30 min. During the process the baths were stirred at 300 rpm.

The list of obtained materials is given in Table 2. Current density equal to 2.5 A/dm<sup>2</sup> in both DC and PC modes was used. In the PC mode, 100 Hz frequency 50% duty cycle was investigated. The composites and alloys were deposited using coulometric conditions (60 C/cm<sup>2</sup>).

The zeta potential ( $\zeta$ ) of the nc-TiO<sub>2</sub> suspended in the electrolytic bath was measured using a ZetaSizer Nano-ZS 90 (Malvern, USA). The measurements were performed in diluted 50 times electrolytic bath on 3 samples. For each sample three series of at least 10 measurements each were carried out.

Roughness parameters of the external surfaces of the electrodeposited materials were measured by a Wyko NT930 optical profilometer (Veeco, USA).  $R_a$  (arithmetical average of the absolute values of the profile heights deviations),  $R_q$  (root mean square roughness) and  $R_t$  (maximum height of the profile) were calculated from the roughness profiles.

Microhardness was measured on the polished surfaces of longitudinal cross-sections of the electrodeposited materials using a TUKON 2500 microhardness tester (Wolpert-Wilson, USA) with a Vickers indenter under a load equal to 0.3 N. For each sample, the average microhardness of a minimum of 10 measurements was determined.

For investigation of surface morphology and microstructure, Inspect S50 and Nova NanoSEM 450 (FEI, USA) scanning electron microscopes (SEM) were used. SEM images were acquired using detectors of secondary electrons (SE) and backscattered electrons (BSE). Moreover, a concentric backscatter detector (CBS) was used to investigate the microstructural features in complementary topographical (SE) and compositional (BSE) contrasts. Transmission and scanning-transmission electron microscopy (TEM, STEM) investigations were carried out using JEM-2010 ARP (Jeol, Japan) and Tecnai Osiris (FEI, USA) microscopes. STEM images were acquired in the high angle annular dark-field (HAADF) mode. Microanalysis of the chemical composition was performed by means of energy dispersive X-ray

spectroscopy (EDS) in SEM and STEM. The sum spectra acquired while scanning the total area of 5820  $\mu\text{m}^2$  in SEM with a dwell time of 2 ms allowed the peak-to-background ratio of the Ti K $\alpha$  peak of at least 2:1 to be obtained, and thus quantitative EDS microanalysis of Ni, Fe and Ti to be performed. The concentration of TiO<sub>2</sub> in wt% was approximated based on the Ti content in accordance with oxide stoichiometry. For selected specimens, the local chemical composition was examined using EDS in STEM. EDS elemental maps were acquired in the STEM mode using a ChemiSTEM™ system of four silicon drift (SDD) detectors.

X-ray diffraction (XRD) and selected area electron diffraction (SAED) patterns were used to determine the phase composition of electrodeposited materials. SAED patterns were analysed using JEMS v4.4230 software (Pierre Stadelmann, JEMS-SAS, Switzerland). XRD patterns were acquired using a Panalytical Empyrean DY 1061 (Malvern Panalytical, USA) diffractometer in Bragg–Brentano geometry with the use of Cu K $\alpha$  radiation ( $\lambda = 0.154$  nm). A PDF-4+ (product of ICDD, USA) database was used for phase identification. The size of crystallites was measured using the Scherrer equation with the most intense peak for each phase. The effective depth of X-ray penetration, determined based on Eq. (1), was equal to 4.5  $\mu\text{m}$ , where  $G_x$  is the assumed fraction of the total X-ray diffracted intensity, which is absorbed by the surface layer of depth  $z$ , and  $\mu$  is the linear absorption coefficient.

$$z = \frac{\ln \frac{1}{1-G_x}}{2\mu} \sin \theta \quad (1)$$

Image analysis and stereological measurements of the equivalent circle diameter (ECD) of grains and volume fraction of nc-TiO<sub>2</sub> in composites were performed with ImageJ 1.50i software (ImageJ, USA). The size distributions of grain ECD were determined based on measurements taken on TEM bright-field images with a total area equal to 0.3  $\mu\text{m}^2$  for each material examined. The volume fraction of nc-TiO<sub>2</sub> particles was determined using SEM CBS images with a total area equal to 1970  $\mu\text{m}^2$  for each sample, using a systematic manual point counting method. The total number of 1600 points ( $P_T$ ) for each composite was used. The measurement error  $\delta$  was calculated using Eq. (2) [20], where  $P_P$  is the estimator of the volume fraction of nc-TiO<sub>2</sub> particles:

$$\delta = \sqrt{\frac{\bar{P}_P(1 - \bar{P}_P)}{P_T \cdot \bar{P}_P}} \quad (2)$$

Magnetic properties were measured using a superconducting quantum interference device (SQUID) magnetometer (Quantum Design, MPMS) by applying an external field of up to 4 T in plane and out of plane of the sample. The

**Table 2** The list of electrodeposited composites and alloys with the current conditions indicated

Acronym	Alloy/composite	Current conditions	Current density (A/dm <sup>2</sup> )
NF-DC	Ni–Fe	DC	2.5
TNF-DC	nc-TiO <sub>2</sub> /Ni–Fe	DC	2.5
NF-PC	Ni–Fe	PC 50%	2.5
TNF-PC	nc-TiO <sub>2</sub> /Ni–Fe	PC 50%	2.5

magnetic measurements were carried out at the temperatures of 300 K and 5 K.

### 3 Results and Discussion

#### 3.1 $\zeta$ Potential of nc-TiO<sub>2</sub> Particles in the Electrolytic Bath

The electrophoretic mobility of nc-TiO<sub>2</sub> particles in the presence of Ni and Fe ions was investigated using measurements of  $\zeta$  potential in the electrolytic bath with the composition given in Table 1. The  $\zeta$  potential of nc-TiO<sub>2</sub> particles was equal to  $8.4 \pm 3.2$  mV. The obtained results revealed that suspended nc-TiO<sub>2</sub> particles in a diluted electrolytic bath are characterized by a positive charge, which enables their electrophoretic movement towards the cathode. The stability of the suspension was rather poor and nc-TiO<sub>2</sub> particles sedimented completely after 30 min without stirring. Therefore, in order to obtain a more homogeneous concentration of suspended particles in the whole volume of the electrolytic bath and prevent the sedimentation of particles, magnetic stirring was applied.

#### 3.2 Chemical Composition

The chemical composition of Ni–Fe alloys and nc-TiO<sub>2</sub>/Ni–Fe composites determined using EDS microanalysis in SEM is given in Table 3. The deposited composites were characterized by higher concentrations of Fe than in the electrolytic bath from which they were obtained, which shows the anomalous character of electrodeposition.

In the Ni–Fe alloys deposited under DC (NF-DC) and PC (NF-PC) conditions, the weight ratio of Ni:Fe was equal to 2.0 and 1.5, respectively. Meanwhile, for the composites deposited under DC (TNF-DC) and PC (TNF-PC) conditions, the Ni:Fe ratio was equal to 2.1 and 2.2, respectively. The differences in chemical compositions can be explained on the basis of previously published studies. There are several theories about the influence of PC conditions on the chemical composition of the electrodeposited Ni–Fe matrix. In many cases, specific PC conditions can increase

the concentration of Fe in alloys, which was confirmed by Zubar et al. [21]. In that work, a higher concentration of Fe in Ni–Fe alloys was obtained in the frequencies lower than 500 Hz and duty cycle equal to 50%. Moreover, in Ni–Fe-based nanocomposites with a higher density of grain boundaries, the Fe concentration should be higher [21]. On the other hand, close to the working electrode, the concentration of Fe<sup>2+</sup> becomes depleted as a result of an anomalous reduction of Fe ions [22]. Under PC conditions where the off-time is longer, the concentration of Fe<sup>2+</sup> faster aligns in the whole volume of the electrolyte, which leads to a higher concentration of Fe<sup>2+</sup> in the interface area than in DC conditions. The different chemical composition of the electrolytic bath in the interface area is probably the main reason for the chemical composition differences between PC and DC alloys.

In composite materials, the change in chemical composition caused by the change in current conditions from DC to PC was negligible. This might be connected with disorder by nc-TiO<sub>2</sub> particles hydrodynamic parameters during the deposition of alloys equivalent to the composite matrix and similar grain size distribution in TNF-DC and TNF-PC, which is described later in the *Microstructure* subsection.

The concentration of nc-TiO<sub>2</sub> in TNF-PC was higher ( $5.8 \pm 0.8$  wt%) than in the TNF-DC composite ( $4.4 \pm 0.8$  wt%), which demonstrated that PC conditions were also beneficial for the co-deposition of nc-TiO<sub>2</sub>. Many researchers noticed that, in off-time under PC electrodeposition, better particle adsorption on the working electrode surface occurs, which is related to a higher amount and better connection of incorporated particles in electrodeposited alloys than under DC conditions [23–25]. It may be postulated therefore that, in our experiments, cyclic depolarization of the working electrode enhanced the nc-TiO<sub>2</sub> deposition.

The amount of incorporated nc-TiO<sub>2</sub> in nc-TiO<sub>2</sub>/Ni–Fe composites obtained in this study is similar to the amounts in other reports about the co-deposition of nc-TiO<sub>2</sub>. Danilov et al., in electrodeposited nc-TiO<sub>2</sub>/Fe composites, obtained concentrations of nc-TiO<sub>2</sub> in the range 2.0–6.0 wt%, depending on the concentration of nanoparticles in the bath and current density [26]. Mohajeri et al. [27], using PC conditions, incorporated more than 11 wt% of sol–gel synthesized TiO<sub>2</sub> particles in the Ni matrix.

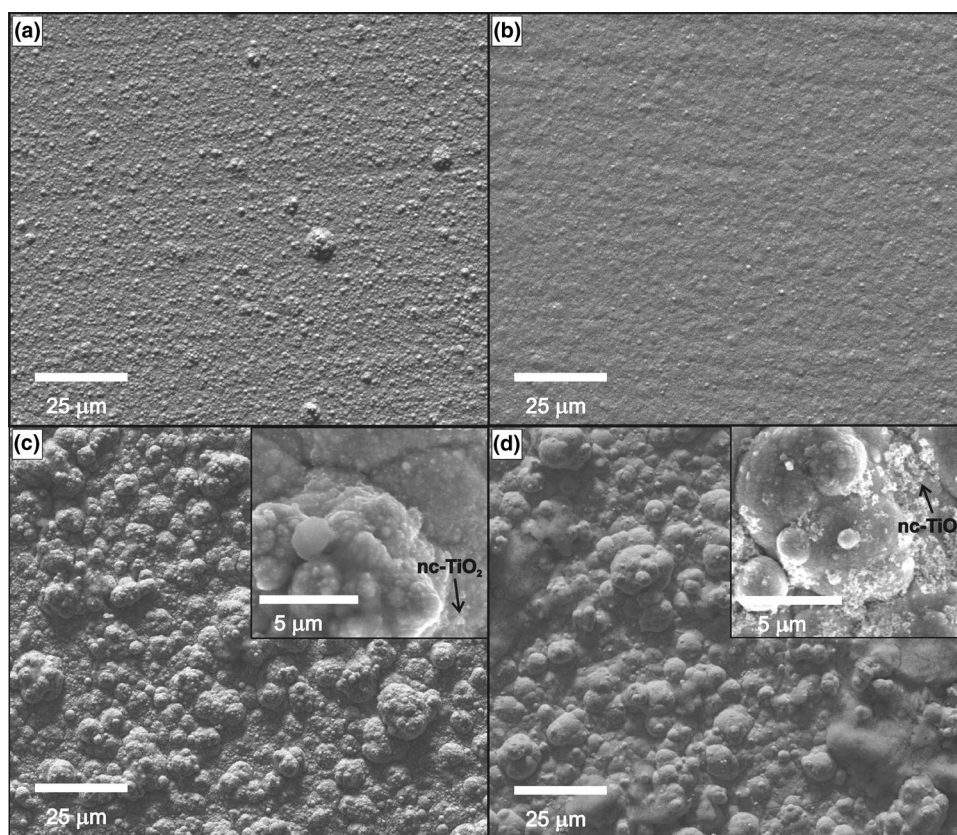
#### 3.3 Surface Morphology and Roughness

Figure 1a–d show SEM images of the surface morphology of the deposited alloys and composites. The surfaces of NF-DC and NF-PC exhibited typical nodular morphology as shown in the insets in Fig. 1a, b. Addition of nc-TiO<sub>2</sub> particles significantly influenced the formation of cauliflower structures. The change of surface morphology of electrodeposited Ni–Fe-based composites, as compared to parent alloys, is characteristic not only for those containing nc-TiO<sub>2</sub>. It

**Table 3** Chemical composition of the obtained Ni–Fe alloys and nc-TiO<sub>2</sub>/Ni–Fe composites determined by EDS in SEM

Alloy/composite	Element Concentration ± SD (wt.%)			
	Ni	Fe	Ni:Fe ratio	TiO <sub>2</sub>
NF-DC	66.6 ± 0.5	33.4 ± 0.5	2.0	0
NF-PC	60.1 ± 0.3	39.9 ± 0.3	1.5	0
TNF-DC	65.0 ± 0.8	30.6 ± 0.6	2.1	4.4 ± 0.7
TNF-PC	64.8 ± 1.7	29.4 ± 0.7	2.2	5.8 ± 0.8

**Fig. 1** Surface morphology of the electrodeposited alloys and composites: **a** NF-DC, **b** NF-PC, **c** TNF-DC, **d** TNF-PC, SEM SE images. TiO<sub>2</sub> agglomerates are marked on enlarged images in (c and d)



was reported that also incorporation of ZrO<sub>2</sub> nanoparticles into the Ni–Fe matrix provides to obtain granular surface morphology [11]. On the surface of electrodeposited composites, agglomerates of nc-TiO<sub>2</sub> were observed (Fig. 1c, d). TNF-PC was characterized by a smoother surface morphology than TNF-DC, which was confirmed by roughness measurements using an optical profilometer (Fig. 2). The values of the  $R_a$ ,  $R_t$ , and  $R_q$  parameters are given in Table 4. It was observed that values of the roughness parameters were lower for Ni–Fe alloys than for nc-TiO<sub>2</sub>/Ni–Fe composites. It was also seen that the PC conditions caused a significant decrease in the surface roughness of electrodeposited materials.

There are several concepts explaining the influence of oxide and/or nitride particles on the surface morphology of Ni–Fe-based composites. Chaudhari and Singh [28] showed that the incorporation of In<sub>2</sub>O<sub>3</sub> nanoparticles during the electrodeposition of Ni–Fe leads to a decrease in the surface roughness due to the reduction in grain size. On the contrary, other studies indicated that Al<sub>2</sub>O<sub>3</sub> [29] or Si<sub>3</sub>N<sub>4</sub> [30] particles influence the increased roughness of the electrodeposited Ni–Fe composites. The literature also reports that PC conditions allow smoother surfaces of electrodeposited composites to be obtained when compared with those achieved in DC conditions [21]. Zubar et al. [21] noticed that using high frequency PC electrodeposition

results in Ni–Fe alloys with low porosity, defect-free microstructures and lower roughness than under DC conditions. Therefore, our further studies were focused on the qualitative and quantitative microstructural characterization of deposited alloys and composites to examine the influence of deposition conditions on the microstructural parameters of nc-TiO<sub>2</sub>/Ni–Fe composites, and thus the surface morphology.

### 3.4 X-ray Diffraction Analysis

In Fig. 3, the XRD patterns of the NF-DC, NF-PC, TNF-DC and TNF-PC samples are shown. The phase identification was based on the JCPDS base card 04-003-2245 for Ni–Fe alloy. Intensities of XRD peaks for the used standard, as well as for examined specimens, are collected in Table 5. The strong (111), (200), (220), (311) and (222) peaks detected in the XRD patterns of NF-DC, NF-PC, TNF-DC and TNF-PC were identified as the Ni–Fe fcc  $\gamma$  phase of the Fm-3 m space group. For NF-PC, all identified peaks were shifted to lower values than in other investigated materials, which was related to the higher concentration of Fe. In all specimens, the coatings grew with the (111) orientation. For the NF-DC alloy, the higher intensity of the (200) peak compared with the standard and a significant decrease in intensities of the remaining peaks were noticed. The application of PC for

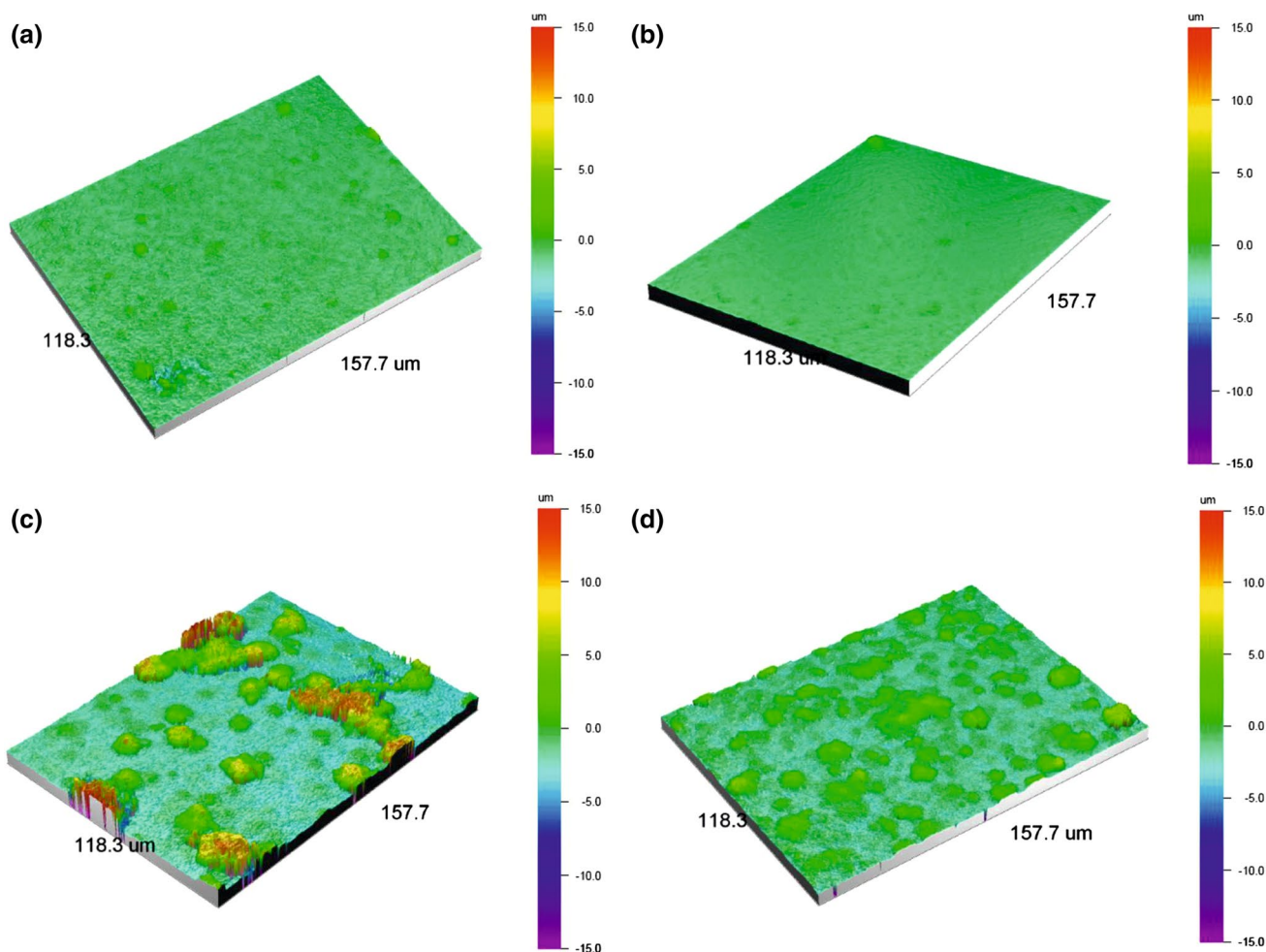


**Fig. 2** Roughness maps of the Ni–Fe alloys and nc-TiO<sub>2</sub>/Ni–Fe composites: **a** NF-DC, **b** NF-PC, **c** TNF-DC, **d** TNF-PC

**Table 4** Roughness parameters of Ni–Fe alloys and nc-TiO<sub>2</sub>/Ni–Fe composites

Parameter (μm)	Alloy/composite			
	NF-DC	NF-PC	TNF-DC	TNF-PC
R <sub>a</sub>	0.23	0.09	2.36	1.64
R <sub>q</sub>	0.48	0.19	3.25	2.12
R <sub>t</sub>	26.27	9.98	26.67	29.08

NF-PC results in the preferred (111) orientation. The XRD pattern of the TNF-DC composite was also characterized by a higher intensity (200) peak, but not as high as for the NF-DC alloy, while the intensities of other peaks were similar to those in the standard. The obtained results indicate a more pronounced orientation texture in the electrodeposited NF-PC alloy than in NF-DC. Similarly, the texture in TNF-PC is more pronounced than in TNF-DC composites.

The obtained results may indicate that PC deposition enhanced the electrocrystallization of grains in the preferred

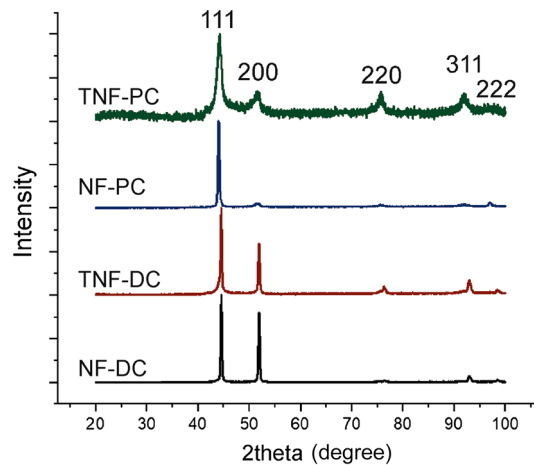


**Fig. 3** XRD patterns of the electrodeposited materials

**Table 5** Intensities of XRD peaks in the Ni–Fe alloy standard, as well as in experimental spectra acquired for the NF-DC, TNF-DC, NF-PC and TNF-PC samples

No.	2theta (°)	Miller indices			Intensity				
		h	k	l	Ni–Fe alloy standard	NF-DC	TNF-DC	NF-PC	TNF-PC
1.	44.49	1	1	1	1	1	1	1	1
2.	51.84	2	0	0	0.418	0.773	0.628	0.037	0.221
3.	76.35	2	2	0	0.164	0.013	0.085	0.020	0.270
4.	92.95	3	1	1	0.146	0.072	0.177	0.021	0.202
5.	98.46	2	2	2	0.04	0.028	0.050	0.050	0.080

orientation. On the other hand, in composites, the addition of nc-TiO<sub>2</sub> particles increases the number of nucleation sites and results in a more random orientation of crystallites. In ordinary crystallization of a fcc structure, the (111) orientation is the preferred orientation due to the higher atom density than in the (200) orientation. In turn, Chaudhari and Singh [11] postulated that the orientation of the Ni–Fe matrix may be associated with the hydrogen evolution. They observed that in ZrO<sub>2</sub>/Ni–Fe composites the (111) orientation is preferred for lower current densities, but for higher current densities, where hydrogen generation is higher, orientation often changes to (220).

Electrocrystallization of grains depends on a number of factors, including those related with the current, such as current density, duty cycle or pulse frequency. PC deposition introduces many perturbations that result in higher desorption of interfacial inhibitors, such as hydrogen and iron or nickel hydroxides from the cathode surface during off-time. This can lead to the formation of a greater number of defects in nickel coatings deposited under higher current frequencies and lower duty cycles [31]. On the other hand, during the co-deposition of Ni with nc-TiO<sub>2</sub> particles, the adsorption/desorption phenomena can occur on the surface of TiO<sub>2</sub> particles, introducing additional perturbation to grain growth [32]. It can therefore be assumed that the presence of many disturbances in grain growth during PC electrodeposition may lead to changes in the preferred orientation of crystallites in electrodeposited Ni–Fe alloys and nc-TiO<sub>2</sub>/Ni–Fe composites.

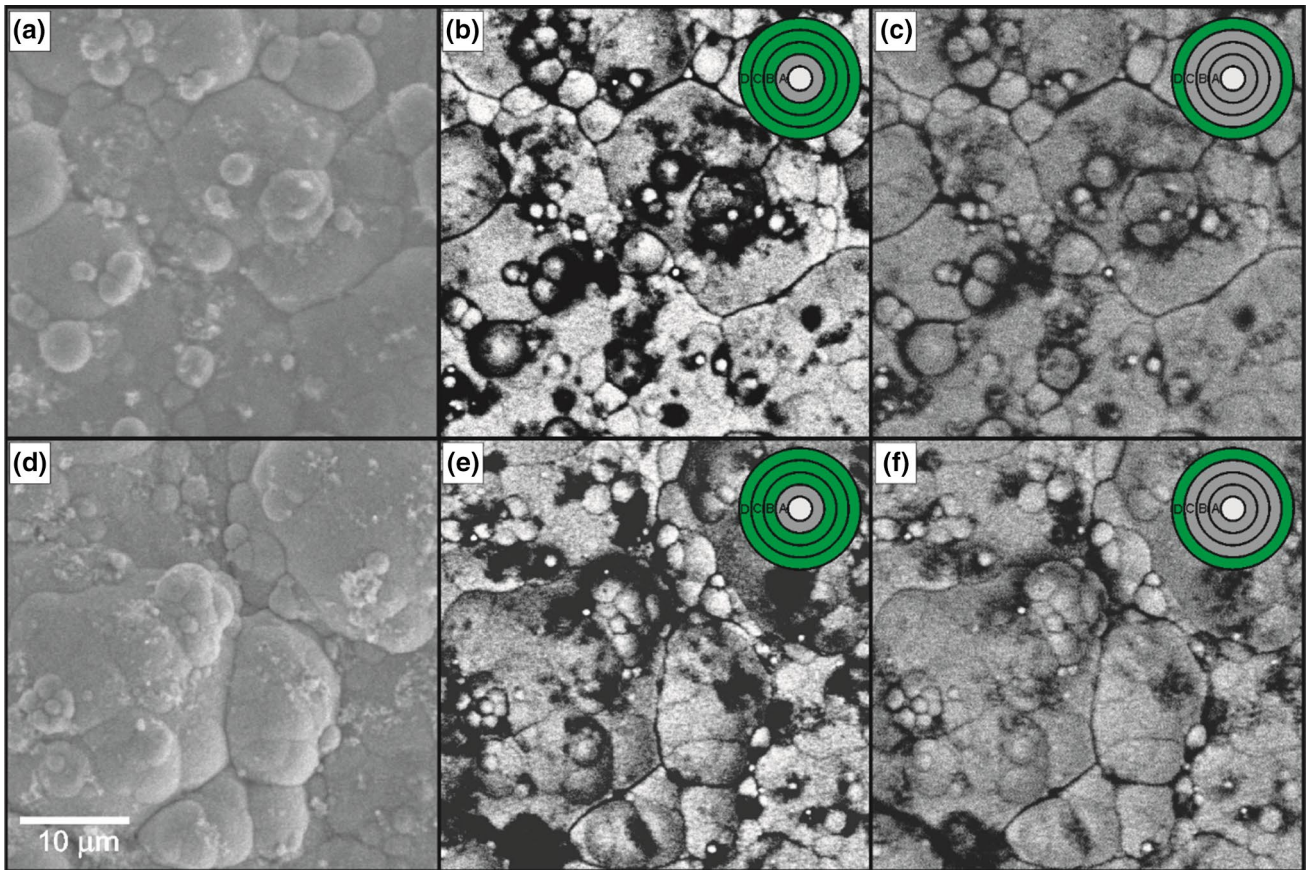
In the XRD patterns of TNF-DC and TNF-PC, no peaks of the nc-TiO<sub>2</sub> phase were resolved. The relatively low concentration and high dispersion of nc-TiO<sub>2</sub> particles in the Ni–Fe matrix prevented their detection by XRD.

### 3.5 Microstructure

Figure 4a–f show the SEM images of the TNF-DC and TNF-PC surfaces acquired using SE and different segments of the CBS detector and thus different take-off angles. Figure 4a, d reveal the SE images, Fig. 4b, e mixed topographical and compositional contrast (rings: B, C, D), while Fig. 4c, f show images in compositional contrast

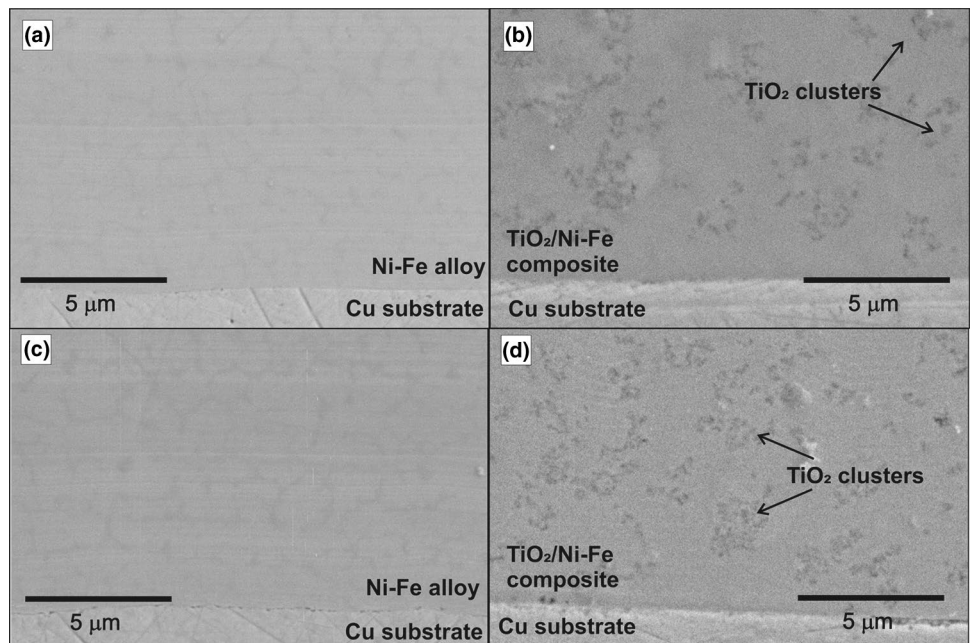
(ring: D). The areas with higher amounts of clusters of nc-TiO<sub>2</sub> particles, containing lighter elements than the Ni–Fe matrix, are visible as darker areas in Fig. 4b–f and, respectively, as objects with a lighter contrast in Fig. 3a, d. The images obtained from the summary signal from the B, C and D rings of the CBS detector are characterized by higher contrasts of nc-TiO<sub>2</sub> particles, but unfortunately they contain dark shadows resulting from the topography of the surface. In the images acquired with the use of the D ring of the CBS detector, the SE component in the detected signal is smaller, which results in a compositional contrast related with the atomic number of chemical elements, without the component from the surface topography. The volume fractions of nc-TiO<sub>2</sub> determined using images taken with the D ring were respectively equal to  $10.6 \pm 2.4\%$  and  $13.4 \pm 2.3\%$  for TNF-DC and TNF-PC, which was in good agreement with EDS measurements. The results of both chemical composition and stereological analysis confirm that the TNF-PC composite is characterized by a higher content of nc-TiO<sub>2</sub> reinforcement. In Fig. 4b–f, partially incorporated nc-TiO<sub>2</sub> clusters are observed as the black areas on the surfaces of both composites, while the particles fully incorporated in the Ni–Fe matrix are visible as grey areas. The distribution of nc-TiO<sub>2</sub> particles was homogeneous on the surface in both TNF-DC and TNF-PC. The estimated volume fractions of nc-TiO<sub>2</sub> particles in the obtained composites are comparable with those reported in other electrodeposited composites reinforced by ceramic nanoparticles [26, 33].

Figure 5a–d shows a typical cross-sectional low-magnification SEM SE images of the NF alloys and TNF composites. It can be seen that the materials exhibit a dense and compact structure. The thickness of the alloys/composites is about 15 μm. The interface between the alloys/composites and the copper substrate is characterized by a very good connection, without visible pores and discontinuities. The agglomerates of nc-TiO<sub>2</sub>, with a darker contrast in the SEM BSE image, are distributed in the Ni–Fe matrix. The nc-TiO<sub>2</sub> agglomerates in TNF-PC were distributed in the form of smaller, but more evenly distributed clusters than in TNF-DC sample. In order to investigate the nc-TiO<sub>2</sub> distribution in TNF-PC, a detailed study was carried out by means of



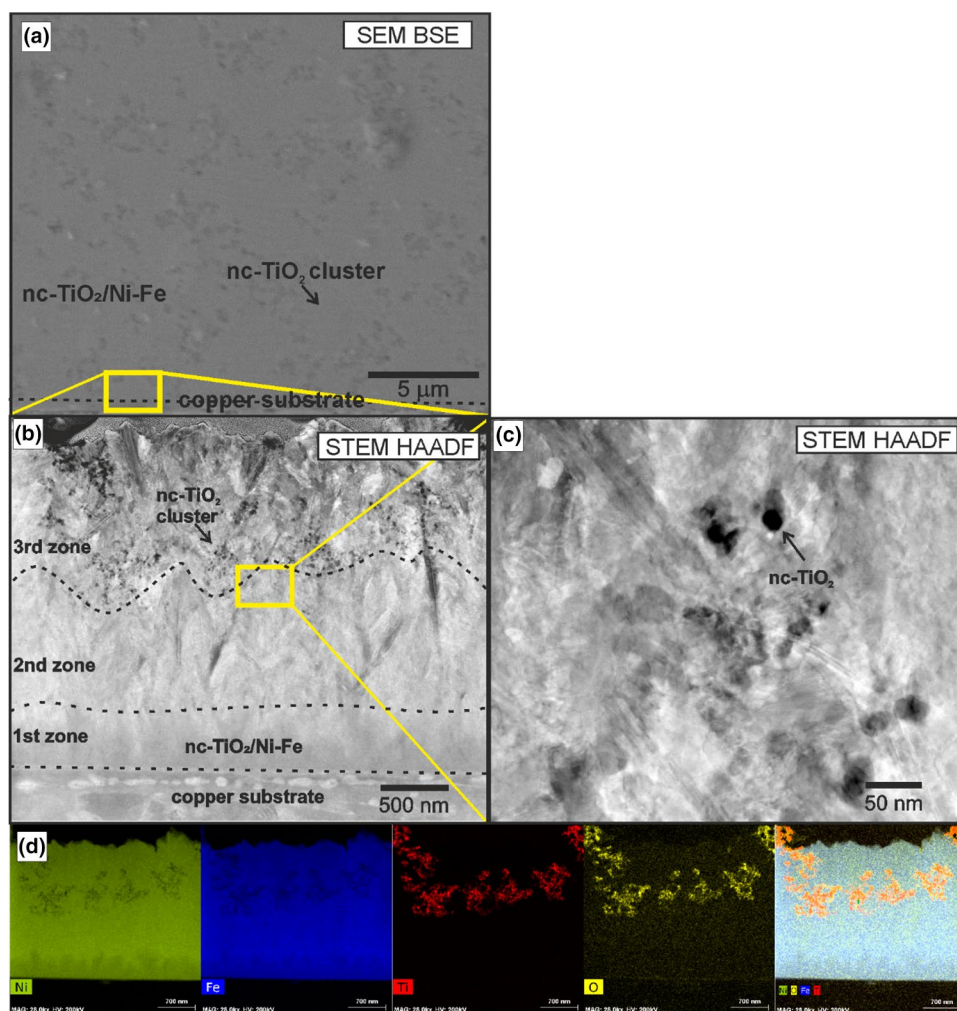
**Fig. 4** SEM images of the surface of **a, b, c** TNF-DC and **d, e, f** TNF-PC composites acquired using the SE detector (**a, d**), CBS detector from the rings: B, C, D (**b, e**) and from the D ring (**c, f**)

**Fig. 5** Microstructure of **a** NF-DC, **b** TNF-DC, **c** NF-PC and **d** TNF-PC observed on cross-section images in SEM BSE. The nc-TiO<sub>2</sub> agglomerates are marked by arrows





**Fig. 6** Microstructure of TNF-PC observed in cross-section images acquired in **a** SEM-BSE and **b, c** STEM-HAADF contrast; the areas shown in enlarged views in subsequent images are marked with yellow rectangles, the examples of nc-TiO<sub>2</sub> agglomerates and isolated nanoparticles are marked by arrows, **d** corresponding EDS elemental maps of Ni, Fe, Ti and O as well as the STEM image with superimposed maps of all analysed elements. (Color figure online)



STEM and EDS elemental maps using FIB lamella prepared from the cross-section of the composite at a location close to the substrate-coating interface in Fig. 6a.

In Fig. 6b, c, a STEM-HAADF micrographs showing the microstructure at the cross section of the composite and the underlying substrate are given. In such an image, the high-angle scattered electrons are captured and the contrast is approximately proportional to the square of the atomic number  $Z^2$ . In the Z-contrast images in Fig. 6b, c, the lower intensity is associated with nc-TiO<sub>2</sub> due to the lower atomic number of Ti compared to Ni and Fe in the matrix. The agglomerates of nc-TiO<sub>2</sub> with a semi-spherical shape are visible.

In Fig. 6b, the differences in the microstructure at the substrate side and internal part of the lamella were observed. Three zones with different grain size and morphology can be recognized and marked in Fig. 6b. On the substrate side, the first zone is the initial layer of fine nanograins with the size of several nanometres. Subsequently, in the second zone, the grain morphology transforms to columnar islands. The width of columns is approximately 100 nm. In both the initial and

columnar zones, clusters of nc-TiO<sub>2</sub> are not observed. Figure 6c shows the higher magnification STEM-HAADF image of the third zone, which is characterized by the randomly oriented islands of fine elongated grains with the size range from several nanometres up to 100 nm. In this zone, TiO<sub>2</sub> nanoparticles with diameters below 30 nm are densely incorporated into the Ni–Fe matrix without any discontinuities at the metal-ceramic interfaces. It may be suspected that the columnar growth in the second zone is disturbed by the incorporation of nc-TiO<sub>2</sub>, which act as nucleation sites of the new grains. As a consequence, the morphology of the coating transforms across the growth direction from columnar into randomly oriented islands. The microstructural features observed in individual zones are specific to electrodeposited Ni-based alloys and composites. The character of each zone might depend on the differences in chemical composition of the deposits and electrodeposition conditions [34].

The elemental distributions of Ni, Fe, Ti and O in the composite, obtained on the EDS maps over the area in the STEM-HAADF image, are given in Fig. 6d. The elemental maps show complementary features. The high intensity

parts of the Ti and O maps correspond to dark areas in the Ni and Fe maps, which is related to the distribution of TiO<sub>2</sub> nanoparticles in the Ni–Fe matrix. This is clearly visible by superimposing the maps onto the structure in the STEM-HAADF image. Agglomerates of TiO<sub>2</sub> nanoparticles appearing in dark contrast are assigned to high intensity pixels in the Ti and O maps. The map of Ti reveals that TiO<sub>2</sub> nanoparticles are not incorporated into the initial and columnar layers. Thus our results show that the differences in chemical composition at the cross section of the coating, associated with the distribution of TiO<sub>2</sub>, apply only to the depletion of TiO<sub>2</sub> agglomerates in the narrow zone of 1.5 μm in thickness in the vicinity of the substrate, thus it can be assumed that the reinforcing particles are homogeneously distributed over the whole 15 μm thick coating. Figures 7 a–d show TEM bright-field images of Ni–Fe alloys and nc-TiO<sub>2</sub>/Ni–Fe composites and corresponding grain size distributions. It can be seen that all the samples exhibit a nanocrystalline structure. Our TEM observations revealed relatively frequent twinning in nanograins (e.g. Fig. 7a). Similarly, a tendency for twinning in electrodeposited Ni was reported by [35]. In Ni-based electrodeposited materials, the twins are perpendicular to the substrate plane and parallel to the long columnar axes. The normal columnar growth is preferred as long as the twinning plane is parallel [36].

The size ranges and mean ECD of grains determined using image analysis, as well as the size of crystallites determined by XRD, are given in Table 6. It was observed on the TEM images that a smaller grain size occurred in NF-PC than in NF-DC. The NF-DC alloy was characterized by a less homogeneous grain size distribution among all the investigated materials, with a broad scatter in the ECD of grains in the range of 38–519 nm and the mean grain diameter equal to 142 nm ± 73 nm. Meanwhile, for the NF-PC alloy, the ECD of grains was significantly lower, i.e. in the range of 10–280 nm, with the mean value equal to 31 nm ± 15 nm. The nc-TiO<sub>2</sub>/Ni–Fe composites were characterized by more homogeneous grain size distribution than Ni–Fe alloys. For the TNF-DC composite, grain diameter is in the range 10–104 nm and the mean value is 31 nm ± 15 nm. The TNF-PC composite exhibits very similar grain size in the range of 5–91 nm and the mean diameter of 27 nm ± 13 nm. In turn, the grain size estimated using the Scherrer equation for the (111) orientation in NF-DC and NF-PC was equal to 38 nm and 29 nm, respectively, while for the TNF-DC and TNF-PC composites it was 29 nm and 10 nm.

In all cases, the size of crystallites estimated by XRD was lower than that determined based on TEM images, but the results obtained by both methods followed the same trend. Those discrepancies between the grain size might be connected with the local character of TEM investigations and lower volume of analysed material than in XRD. The results

of grain size determination using TEM images are also sensitive to the presence of many lattice defects, such as twins, which can break the X-ray coherency [37].

According to the literature, the PC conditions influence the decrease in the grain size by increasing the nucleation rate [12, 38]. As Fig. 7 and Table 6 show, the addition of nc-TiO<sub>2</sub>, as well as deposition under PC, influence the grain size refinement. Our result is in close agreement with the study of Spanou and Pavlatou [32], who indicated that in nc-TiO<sub>2</sub>/Ni composites deposited from a Watts bath the high frequency PC conditions have a positive influence on the reduction of the grain diameter. Other researchers also pointed to the influence of reinforcement particles on the reduction of grain size in Ni–Fe-based composites. In ZrO<sub>2</sub>/Ni–Fe composites deposited in DC conditions, the ECD of grains determined using TEM images was in the range of 50–60 nm, but the XRD method revealed a smaller value of about 11 nm [11]. In addition, the reinforcement of Ni–Fe by In<sub>2</sub>O<sub>3</sub> particles, measured by XRD, reduced the size of crystallites even from 16 nm to 5 nm [28]. In light of the above, the results of our experiments are consistent with the findings of other researchers.

Figures 8a, b show the TEM dark-field images of the TNF-PC and TNF-DC composite and the corresponding to them diffraction pattern in Fig. 8c, respectively. Diffraction rings of Ni, used as the representing phase for phase analysis of the solid solution of Ni and Fe, as well as the TiO<sub>2</sub> anatase phase, are indicated. The dark-field images in Fig. 8a, b, taken in reflections belonging to the (101) TiO<sub>2</sub> (anatase) ring selected by the area of aperture, show nc-TiO<sub>2</sub> particles in the Ni–Fe matrix. Using local TEM observations, the presence of nc-TiO<sub>2</sub> particles was confirmed.

### 3.6 Magnetic Properties

Figure 9a shows the magnetic hysteresis loops of nc-TiO<sub>2</sub> measured at temperatures of 300 K and 5 K with a subtracted diamagnetic contribution related to the holder (the capsules used as holders showed only a diamagnetic signal). It has been observed that, at both temperatures, the samples are ferromagnetic with a well pronounced paramagnetic fraction in the measurement at the low temperature. Both curves show very small coercivity levels increasing from 20 to 44 Oe with decreasing measurement temperature. The RT coercivity is twice as high as that observed by [14], which may be related to the differences in particle size. The values of saturation magnetization equal to 0.034 emu/g and 0.048 emu/g for 300 K and 5 K, respectively, are the same order of magnitude in comparison to [16]. The field (50 Oe) cooled (FC) and zero field cooled (ZFC) curves of temperature dependent magnetization are shown in Fig. 9b. The drastic increase in magnetization below 30 K with decreasing temperature can be attributed to the paramagnetic

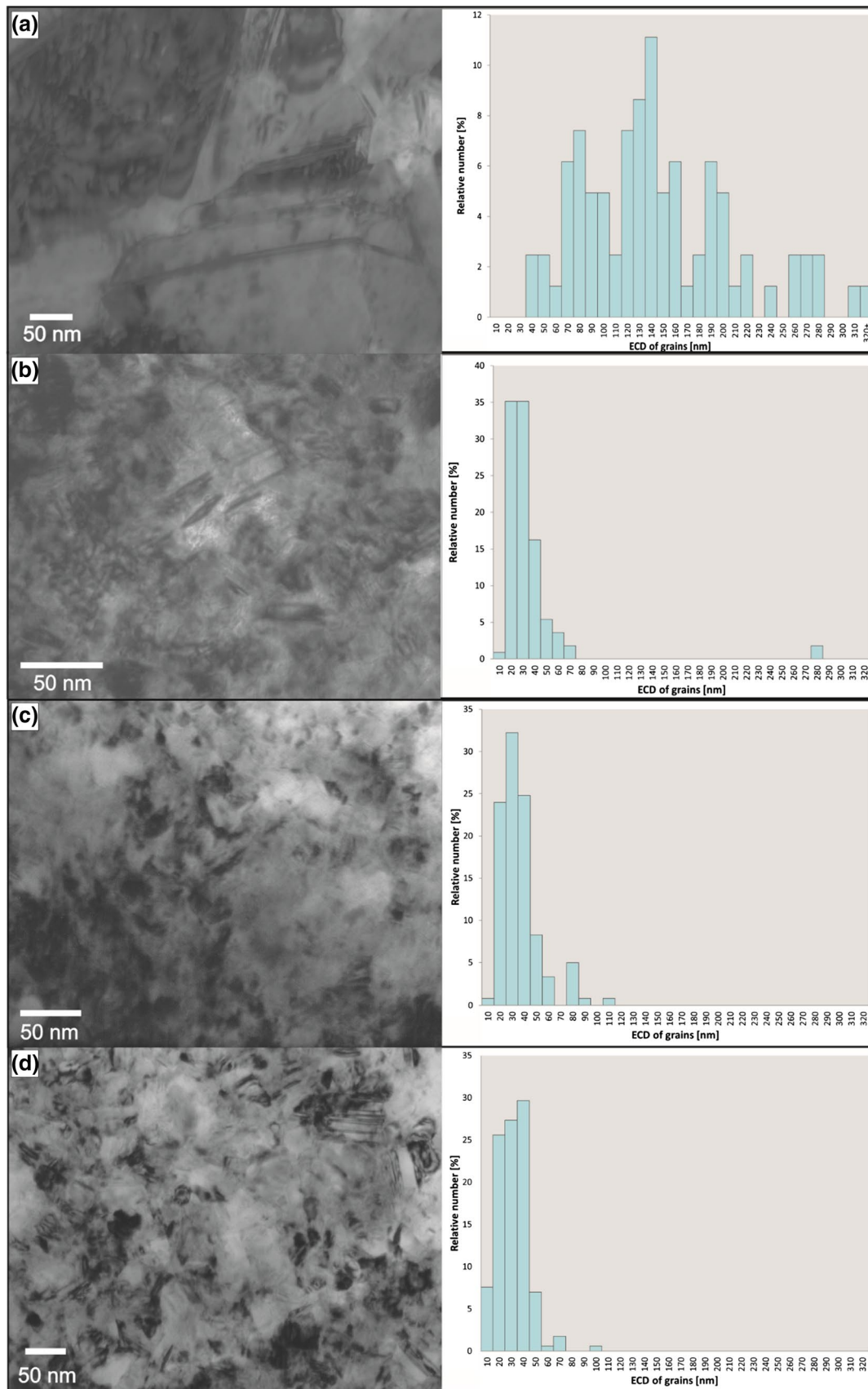


**Fig. 7** TEM bright-field images of the **a** NF-DC, **b** NF-PC, **c** TNF-DC, **d** TNF-PC microstructure and corresponding grain size distributions

**Table 6** Size range and mean ECD of grains with standard deviation as well as volume fraction of nc-TiO<sub>2</sub> determined by XRD and TEM and area fraction of nc-TiO<sub>2</sub> in nc-TiO<sub>2</sub>/Ni-Fe composites

Alloy/composite	Parameter			Area fraction of nc-TiO <sub>2</sub> ± estimation error (%)
	Grain size			
	Determined by TEM		Determined by XRD	
ECD size range (nm)	Mean ECD ± SD (nm)	Mean crystallite size (nm)		
NF-DC	38–519	142 ± 73	38	–
NF-PC	10–280	31 ± 15	29	–
TNF-DC	10–104	31 ± 15	29	10.6 ± 2.4
TNF-PC	5–91	27 ± 13	10	13.4 ± 2.3

**Fig. 8** TEM dark-field images of nc-TiO<sub>2</sub> taken in the (101) ring of TiO<sub>2</sub> (anatase) of **a** TNF-DC and **b** TNF-PC. **c** SAED pattern with its solution for Ni and TiO<sub>2</sub> anatase; the area of selective aperture is marked by a red circle. (Color figure online)

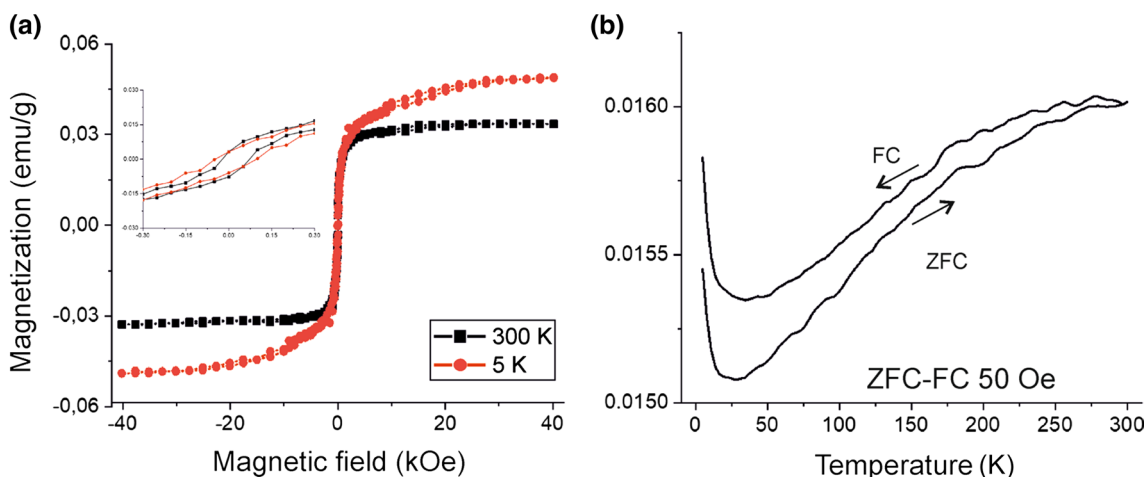
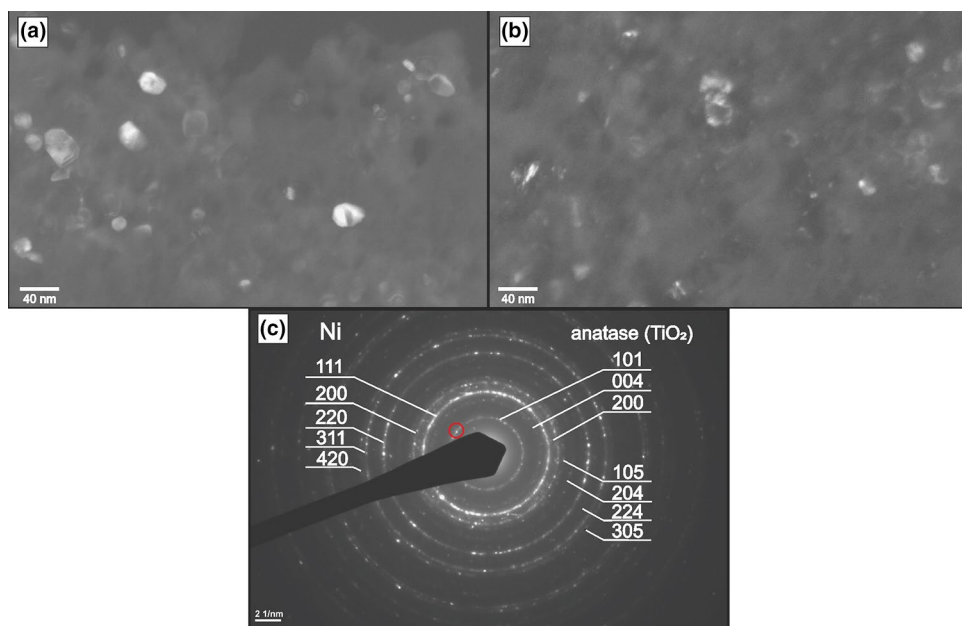


**Fig. 9** **a** Hysteresis loops of nc-TiO<sub>2</sub> nanoparticles measured at 5 K and 300 K and **b** ZFC and FC curves of temperature dependent magnetization of nc-TiO<sub>2</sub> particles

fraction, while clear separation between FC and ZFC indicates ferromagnetic contribution. As previously mentioned in the Introduction, the origin of ferromagnetism is related to defects, especially connected with the presence of Ti and O vacancies.

The magnetic hysteresis loops of NF-DC, NF-PC, TNF-DC and TNF-PC carried out at 300 K are shown in Fig. 10 and the measured values of coercivity ( $H_c$ ) and saturation magnetization ( $M_s$ ) are collected in Table 7. All the investigated materials show ferromagnetic behaviour with high magnetic anisotropy and easy axis along the layer. Hysteresis loops measured in plane indicate low coercivity with values over 10 Oe and saturation magnetization changing from 57.1 emu/g to 137.1 emu/g for TNF-DC and NF-PC, respectively. The  $M_s$  and  $H_c$  values of TNF-DC and TNF-PC are smaller than for the counterparts of the NF-DC and NF-PC alloys.

These results are partially in agreement with those reported by Yousefi et al. [10], who showed that the

**Table 7** Magnetization and coercivity of Ni–Fe alloys and nc-TiO<sub>2</sub>/Ni–Fe composites

	Magnetization $M_s$ (emu/g)	Coercivity $H_c$ (Oe)
NF-DC	80.0	16
NF-PC	134.4	16
TNF-DC	57.1	13
TNF-PC	82.9	12

addition of the nc-TiO<sub>2</sub> phase reduces the  $M_s$  of nc-TiO<sub>2</sub>/Ni–Fe composites. However, our measurements are the opposite to the observations related to  $H_c$  and point to a small decrease in coercivity with the addition of nc-TiO<sub>2</sub>. In turn, our results are consistent with those obtained by Chaudhari et al. [28] who noticed a significant effect of In<sub>2</sub>O<sub>3</sub> nanoparticles on the decrease of coercivity in In<sub>2</sub>O<sub>3</sub>/Ni–Fe composites. It is known that  $M_s$  in Ni–Fe binary

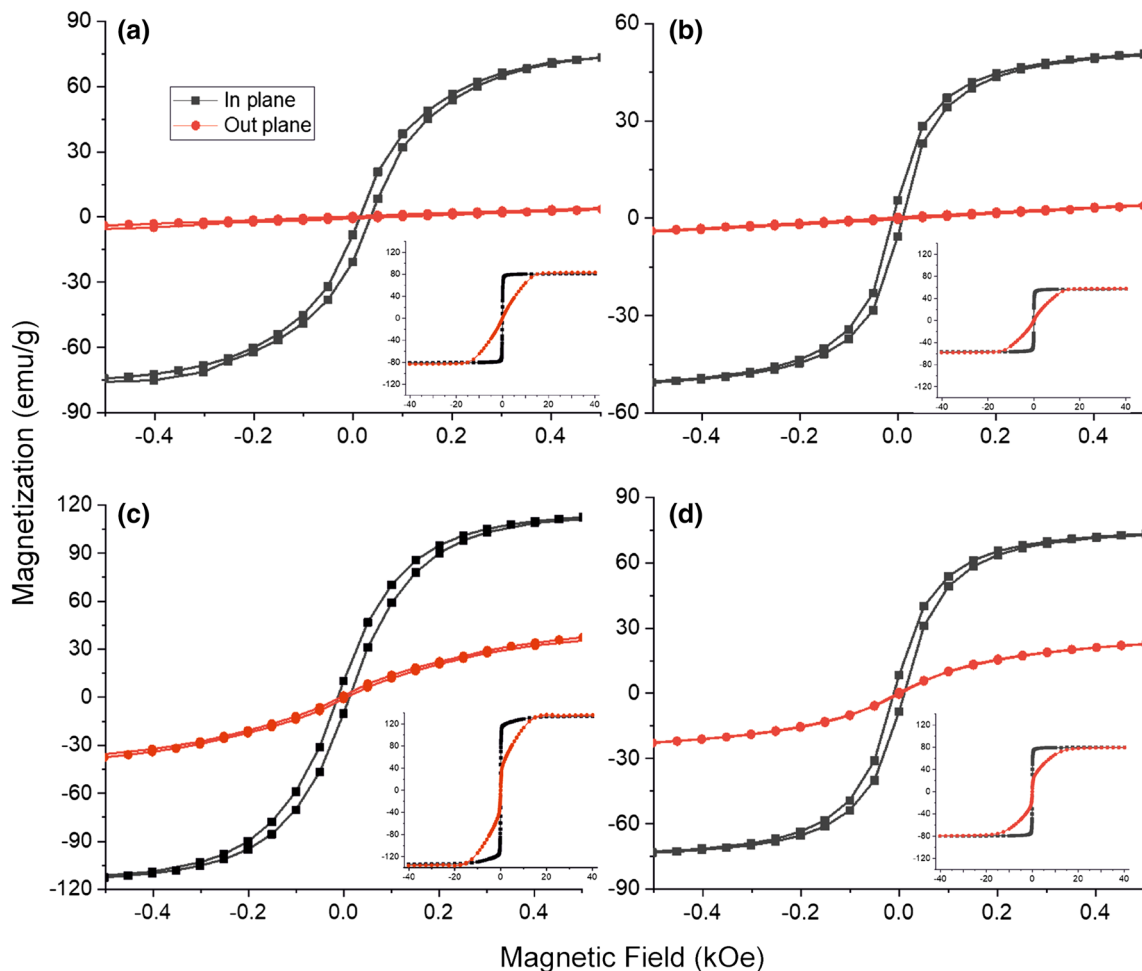


**Fig. 10** Hysteresis loops measured at 300 K in plane (black line) and out plane (red line) geometry for **a** NF-DC, **b** TNF-DC, **c** NF-PC, **d** TNF-PC with the full scan shown in insets. (Color figure online)

**Table 8** Results of microhardness measurements of nc-TiO<sub>2</sub>/Ni–Fe composites, Ni–Fe alloys and copper substrate

Alloy/composite	Hardness (HV0.3)
NF-DC	507 ± 43
NF-PC	463 ± 15
TNF-DC	517 ± 24
TNF-PC	526 ± 16
Copper substrate	91 ± 3

systems decreases with the Ni concentration [39], which is related to the value of saturation magnetization of Ni and Fe equal to 55 emu/g and 217 emu/g, respectively [40]. Thus, a large increase in  $M_s$  for the NF-PC sample can be related to a larger Fe concentration. The magnetic investigations did not show any changes in  $H_c$  between DC and PC deposited materials. On the other hand, the main parameter influencing  $H_c$  is grain size. In nanocrystalline materials, with the grain sizes smaller than the magnetic exchange length ( $L_{ex}$ ), an increase in the density of grain boundaries provides an increase in  $H_c$  [8]. Wang [41] calculated that  $L_{ex}$  is about 14 nm for the Fe–34wt%Ni alloy. Thus, the average ECD of all investigated materials was higher than  $L_{ex}$  for similar materials, which can explain the observed decrease in coercivity for the composites.

### 3.7 Microhardness

The results of microhardness measurements are collected in Table 8. The microhardness results were connected with the chemical composition, microstructure and content of nc-TiO<sub>2</sub> in composites. The hardness of alloys was significantly lower for higher concentrations of Fe in NF-PC. A similar observation connected with the influence of Fe on hardness was presented by Ebrahimi and Li [42]. All of the investigated composites exhibited higher microhardness than the alloys with an analogical Ni:Fe ratio. TNF-PC indicated a higher hardness than the TNF-DC composite, which is probably connected with strengthening by nc-TiO<sub>2</sub> particles. The strengthening of composites is based on the grain size refinement, dispersion of particles and solid solution strengthening [43]. In electrodeposited composites, nc-TiO<sub>2</sub> could act as the blocker of plastic deformation, grain boundary sliding or dislocation movements in composites. A similar effect of hardness improvement was obtained for another metal oxides such as ZrO<sub>2</sub> [11], In<sub>2</sub>O<sub>3</sub> [28], WO<sub>3</sub> [43], as well as micron-sized Si and nano-sized TiO<sub>2</sub> particles [44]. The results of hardness measurements of electrodeposited Ni–Fe alloys reported by [11, 43] were in the range 410–660 HV and these values are consistent with our findings.

## 4 Conclusions

In this work, new nc-TiO<sub>2</sub>/Ni–Fe composites and analogical Ni–Fe alloys were electrodeposited from a single citrate-sulphate bath under DC and PC current conditions. Examinations of the chemical composition, surface morphology, microstructure, microhardness and magnetic properties allowed the differences in the characteristics of composites and alloys to be determined. The obtained results suggest that nc-TiO<sub>2</sub>/Ni–Fe composites might be considered as promising alternative soft ferromagnetic materials for use, for example, as sensors in MEMS devices.

The following conclusions can be drawn from this study:

1. The microstructure, morphology and chemical composition of electrodeposited nc-TiO<sub>2</sub>/Ni–Fe composites, and Ni–Fe alloys equivalent to their matrix, depend on the current conditions. PC conditions are suitable to obtain materials characterized by a finer nanostructure and lower surface roughness than those obtained using DC.
2. nc-TiO<sub>2</sub> co-deposited in the Ni–Fe matrix occurs in the form of isolated nanoparticles and agglomerates several tens of nanometres in size.
3. PC conditions inhibit grain growth and allow the incorporation of a high volume fraction of nc-TiO<sub>2</sub>, exceeding over a dozen percent, which in turn leads to nc-TiO<sub>2</sub>/Ni–Fe composites being obtained with higher hardness than their counterparts deposited using DC.
4. The nc-TiO<sub>2</sub>/Ni–Fe composites exhibit smaller saturation magnetization and coercivity compared with their counterpart alloys.

**Acknowledgements** This work was supported by the AGH-UST (Project No. 15.11.110.509). The Authors acknowledge Dr. Marta Gajewska, ACMiN AGH for FIB specimen preparation.

**Data availability** The raw/processed data required to reproduce these findings cannot be shared at this time as the data also forms part of an ongoing study.

**Open Access** This article is distributed under the terms of the Creative Commons Attribution 4.0 International License (<http://creativecommons.org/licenses/by/4.0/>), which permits unrestricted use, distribution, and reproduction in any medium, provided you give appropriate credit to the original author(s) and the source, provide a link to the Creative Commons license, and indicate if changes were made.

## References

1. M. Schlesinger, M. Paunovic, *Modern Electroplating*, 5th edn. (Wiley, New York, 2010)

2. V. Torabinejad, M. Aliofkhaezrai, S. Assareh, M.H. Allahyarzadeh, A.S. Rouhaghdam, J. Alloys Compd. (2017). <https://doi.org/10.1016/j.jallcom.2016.08.329>
3. H. Dahms, I.M. Croll, J. Electrochem. Soc. **112**, 771 (1954)
4. S. Hessami, C.W. Tobias, J. Electrochem. Soc. (1988). <https://doi.org/10.1149/1.2096238>
5. V. Torabinejad, M. Aliofkhaezrai, A.S. Rouhaghdam, M.H. Allahyarzadeh, Tribol. Int. (2017). <https://doi.org/10.1016/j.triboint.2016.10.025>
6. C. Su, E. Wang, Y. Zhang, F. He, Chang-Wei. J. Alloys Compd. (2009). <https://doi.org/10.1016/j.jallcom.2008.06.050>
7. R. Stefec, Czech J. Phys. (1973). <https://doi.org/10.1007/BF01591208>
8. G. Herzer, IEEE Trans. Magn. (1990). <https://doi.org/10.1109/20.104389>
9. G.P. Pavithra, A.C. Hegde, Appl. Surf. Sci. (2012). <https://doi.org/10.1016/j.apsusc.2012.03.124>
10. E. Yousefi, S. Sharafi, A. Irannejad, J. Alloys Compd. (2018). <https://doi.org/10.1016/j.jallcom.2018.04.232>
11. A.K. Chaudhari, V.B. Singh, Structure. Int. J. Electrochem. Sci. **9**, 7021 (2014)
12. Y.H. Ahmad, A.M.A. Mohamed, Int. J. Electrochem. Sci. **9**, 1942 (2014)
13. X. Wei, R. Skomski, J. Appl. Phys. (2010). <https://doi.org/10.1063/1.3359423>
14. A. Chanda, RSC Adv. (2018). <https://doi.org/10.1039/C8RA00626A>
15. J. Zhao, Z. Ake, W. Zhang, M. Yang, Z. Liu, Optoelectron. Adv. Mater. Rapid Commun. **7**, 393 (2013)
16. K.M. Yin, H.J. Hong, Trans. Inst. Met. Finish. (1997). <https://doi.org/10.1080/00202967.1997.11871140>
17. M. Naeem, S. Qaseem, I. Ahmad, M. Maqbool, J. Nanoparticle Res. (2012). <https://doi.org/10.1007/s11051-012-0808-6>
18. Q. Xu, S. Zhou, H. Schmidt, J. Alloys Compd. (2009). <https://doi.org/10.1016/j.jallcom.2009.08.033>
19. P. Ledwig, M. Kot, T. Moskalewicz, B. Dubiel, Arch. Metall. Mater. (2017). <https://doi.org/10.1515/amm-2017-0063>
20. J. Ryś, *Stereologia Materiałów*, 1st edn. (FOTOBIT-DESIGN, Kraków, 1995)
21. T.I. Zubar, S.A. Sharko, D.I. Tishkevich, N.N. Kovaleva, D.A. Vinnik, S.A. Gudkova, E.L. Trukhanova, E.A. Trofimov, S.A. Chizhik, L.V. Panina, S.V. Trukhanov, A.V. Trukhanov, J. Alloys Compd. (2018). <https://doi.org/10.1016/j.jallcom.2018.03.245>
22. V. Torabinejad, M. Aliofkhaezrai, A.S. Rouhaghdam, M.H. Allahyarzadeh, Wear (2017). <https://doi.org/10.1016/j.wear.2017.03.013>
23. N.P. Wasekar, S.M. Latha, M. Ramakrishna, D.S. Rao, G. Sundararajan, Mater. Des. (2016). <https://doi.org/10.1016/j.matdes.2016.09.070>
24. W.E.G. Hansal, G. Sandulache, R. Mann, P. Leisner, Electrochim. Acta (2013). <https://doi.org/10.1016/j.electacta.2013.08.182>
25. Y. Zhang, D.G. Ivey, Mater. Chem. Phys. (2018). <https://doi.org/10.1016/j.matchemphys.2017.10.043>
26. F.I. Danilov, A.V. Tsurkan, E.A. Vasil'eva, V.S. Protsenko, Int. J. Hydrogen Energy (2016). <https://doi.org/10.1016/j.ijhydene.2016.02.112>
27. S. Mohajeri, A. Dolati, M. Ghorbani, Surf. Coat. Technol. **262**, 173–183 (2015). <https://doi.org/10.1016/j.surfcoat.2014.12.042>
28. A.K. Chaudhari, V.B. Singh, J. Electrochem. Soc. (2015). <https://doi.org/10.1149/2.0271508jes>
29. R. Starosta, A. Zielinski, J. Mater. Process. Technol. (2004). <https://doi.org/10.1016/j.jmatprotec.2004.09.068>
30. Y. Marita, I.I. Yaacob, Proc. World Congr. Eng. **II**, 7 (2008)
31. C. Kollia, N. Spyrellis, Z. Campus, J. Appl. Electrochem. (1990). <https://doi.org/10.1007/BF01019584>
32. S. Spanou, E.A. Pavlatou, J. Appl. Electrochem. (2010). <https://doi.org/10.1007/s10800-010-0080-3>
33. Y. Zhang, D.G. Ivey, Mater. Chem. Phys. (2018). <https://doi.org/10.1016/j.matchemphys.2017.10.043>
34. Y.D. Gamburg, Z. Giovanni, *Theory and Practice of Metal Electrodeposition* (Springer, New York, 2011). <https://doi.org/10.1007/978-1-4419-9669-5>
35. K.S. Kumar, S. Suresh, M.F. Chisholm, J.A. Horton, P. Wang, Acta Mater. (2003). [https://doi.org/10.1016/S1359-6454\(02\)00421-4](https://doi.org/10.1016/S1359-6454(02)00421-4)
36. V.G. Shadrow, T.A. Tochitskii, A.V. Boltushkin, Cryst. Res. Technol. (1993). <https://doi.org/10.1002/crat.2170280205>
37. T. Kolonits, P. Jenei, B.G. Tóth, Z. Czígány, J. Electrochem. Soc. (2016). <https://doi.org/10.1149/2.0911603jes>
38. A. Sharma, S. Bhattacharya, S. Das, K. Das, Metall. Mater. Trans. A Phys. Metall. Mater. Sci. (2014). <https://doi.org/10.1007/s11661-014-2389-8>
39. S. Vitta, A. Khuntia, G. Ravikumar, D. Bahadur, J. Magn. Magn. Mater. (2008). <https://doi.org/10.1016/j.jmmm.2007.05.021>
40. H. Danan, A. Herr, A.J.P. Meyer, J. Appl. Phys. (1968). <https://doi.org/10.1063/1.2163571>
41. M. Wang, Magnetic Properties of Electrodeposited Nanocrystalline Ni–Fe Alloys. A master thesis, McMaster University, 2012
42. F. Ebrahimi, H.Q. Li, Rev. Adv. Mater. Sci. **5**, 134 (2003)
43. A.K. Chaudhari, V.B. Singh, Surf. Coat. Technol. (2016). <https://doi.org/10.1016/j.surfcoat.2016.09.072>
44. M.H. Sarafrazi, M. Alizadeh, J. Alloys Compd. (2017). <https://doi.org/10.1016/j.jallcom.2017.05.223>

**Publisher's Note** Springer Nature remains neutral with regard to jurisdictional claims in published maps and institutional affiliations.